Hybridization of short glass fiber polypropylene composites with nanosilica and graphite nanoplatelets

Diego Pedrazzoli and Alessandro Pegoretti

Journal of Reinforced Plastics and Composites 2014 33: 1682 originally published online 14 July 2014
DOI: 10.1177/0731684414542668

Original Article

JOURNAL OF REINFORCED PLASTICS & COMPOSITES

Journal of Reinforced Plastics and Composites
2014, Vol. 33(18) 1682–1695

DOI: 10.1177/0731684414542668
jrp.sagepub.com
SAGE

Hybridization of short glass fiber polypropylene composites with nanosilica and graphite nanoplatelets

Diego Pedrazzoli and Alessandro Pegoretti

Abstract

The effects of various types and amounts of fumed silica and graphite nanoplatelets on the microstructure and thermomechanical properties of polypropylene composites containing 5, 10, and 20 wt% of short glass fibers have been analyzed. Hybrid composites were produced by melt compounding and compression molding. The aspect ratio of the short glass fiber decreased with the fiber loading and the nanofiller amount. The tensile strength and elastic modulus increased, while the elongation at break decreased as the content of both short glass fiber and nanofiller increased. A two-population model, based on the Halpin–Tsai and Tsai–Pagano composite theories, was used to predict the elastic modulus of the nano-micro hybrid composites. Experimental values appear to be reasonably consistent with model predictions. Tensile energy to break under impact conditions increased with the short glass fiber content but decreased with nanofiller amount. Moreover, storage modulus and creep stability were remarkably enhanced in short glass fiber composites by the presence of both nanofillers.

Keywords

Short fiber composites, hybrid composites, silica, graphite, interface/interphase, mechanical properties

Introduction

Short glass fiber (SGF) reinforced polymer composites are widely used in a growing number of applications in technical and consumer products requiring good thermomechanical properties. The degree of reinforcement provided by the fibers is largely governed by the fiber properties and their concentration, aspect ratio, orientation, dispersion, and by the fiber–matrix adhesion.[1] In most cases, high loadings of SGF are required to achieve the desired performances; this leads to an undesirable increase in specific gravity and brittleness, and reduced processability (melt flow rate).

Polypropylene (PP) is one of the most widely used thermoplastic matrices for the preparation of SGF reinforced composites.[2] In general, short fiber reinforced composites are less resistant to mechanical loads and fatigue damages than the corresponding continuous fiber reinforced materials, mainly because the weak matrix has to sustain a greater proportion of the load.[3] On the other hand, polymer nanocomposites based on nanofillers such as silica, expanded graphite, and carbon nanotubes have recently attracted great interest due to the considerable enhancement in stiffness reached at very low filler loadings.[4–9] Moreover, substantial improvements in mechanical,[10,11] thermal,[12,13] and flammability[14] properties have been reported, while maintaining similar density and optical properties to those of the neat polymer matrix.[15] Furthermore, there are some indications that nanoparticles could play a beneficial role on the interfacial properties of structural composites.[16,17]

Although polymer nanocomposites exhibit improved thermal and mechanical properties at very low filler contents, loadings of more than 10 wt% usually lead to poor dispersion and processing characteristics.[18] Nevertheless, glass fiber loadings of 30–50 wt% are

Department of Industrial Engineering and INSTM Research Unit, University of Trento, Trento, Italy

Corresponding author:
Alessandro Pegoretti, Department of Industrial Engineering and INSTM Research Unit, University of Trento, Trento, 38123, Italy.
Email: alessandro.pegoretti@unitn.it

quite common.[19,20] It is of great interest to explore whether combining two fillers of rather different size scales (i.e. micro- and nano-scale) would improve the performances at low to intermediate filler loadings. Only few preliminary studies have been reported on the structure and properties of glass fiber reinforced polymer nanocomposites.[21–23] The aim of this study is to investigate how the morphology and the mechanical properties of short glass fiber reinforced PP nanocomposites are affected by the combined effect of nanofiller and reinforcing fibers.

Experimental section

Materials and samples preparation

The matrix of the composite samples used in this work was an isotactic homopolymer PP (Melt Flow Index (MFI) at 190°C and 2.16 kg = 6.9 g/10 min, density = 0.904 g/cm^3) produced by Polychim Industrie S.A.S. (Loon-Plage, France) and provided by Lati Industria Termoplastici S.p.A (Varese, Italy) with the commercial code PPH-B-10-FB. Fusabond® P M-613-05 maleic anhydride modified polypropylene (PPgMA) (MFI at 190°C and 2.16 kg = 106.8 g/10 min, density = 0.903 g/cm^3, maleic anhydride content = 0.35–0.70 wt%) was supplied by DuPont™ de Nemours (Geneva, Switzerland).

Both untreated and surface treated fumed silica nanoparticles were supplied by Evonik Industries A.G. (Hanau, Germany). Untreated nanoparticles (Aerosil® A380) had an average primary particle size of 7 nm and a specific surface area of 321 ± 3 m^2/g, as determined by Brunauner-Emett-Teller (BET) analysis.[24] Dimethyldichlorosilane functionalized silica nanoparticles (Aerosil® R974) were characterized by an average primary particle size of 12 nm and a BET specific surface area of 124 ± 1 m^2/g. Silica nanoparticles were dried for 24 h at 100°C before to be used for nanocomposite production. Exfoliated graphite nanoplatelets xGnP®-M-5 have been supplied by XG Sciences Inc. (East Lansing, USA). This filler is characterized by platelets with an average diameter of ~5 μm and thickness in the range of 10–20 nm. Details on the exfoliation process as well as on the morphology of xGnP can be found elsewhere.[25]

Continuous E-glass rovings, designed as RO99 P319, were supplied by Saint-Gobain Vetrotex (Chambèry Cedex, France) and used as received. These glass fibers are surface treated with a silane-based coupling agent specifically designed for PP matrices. SGFs (single fiber diameter = 15.3 ± 1.5 μm, average length = 6.50 ± 0.44 mm) were obtained by chopping the continuous roving by a chopper gun CDA-08 provided by GlasCraft (Graco®, Bury, England).

In previous works of this research group, an evaluation of the fiber/matrix interfacial shear strength (ISS) was performed by the single-fiber fragmentation test (SFFT) on glass fiber microcomposites whose PP matrix was filled with various types and amounts of silica nanoparticles and graphite nanoplatelets.[16,17] The nanocomposite matrices which exhibited the highest ISS values were selected in order to produce SGF composites through melt mixing in a Thermo Haake internal mixer (temperature = 190°C, rotor speed = 50 r/min, time = 10 min). Plane square plaques with a thickness of around 0.7 mm (or 2.7 mm for fracture toughness test) were then obtained by compression molding using a Carver hot press (temperature = 190°C, pressure = 0.76 MPa, time = 10 min).

Composites were designated by indicating the matrix, the compatibilizer (if any) with its content, the kind of filler with its amount, and the glass fibers (GF) amount. For instance, the composite based on unfilled matrix loaded with 5 wt% GF was denoted as PP/GF-5. On the other hand, a sample filled with 5 wt% of PPgMA, 5 wt% of Aerosil® A380, and 20 wt% GF was indicated as PP-PPgMA-5-A380-5/GF-20.

Experimental techniques

Morphology characterization. Transmission electron microscopy (TEM) was adopted to analyze cryocut thin sections of PP nanocomposites. A Philips® EM 400 T (Amsterdam, Netherlands) transmission electronic microscope was used at an acceleration voltage of 120 kV. Samples were prepared by cutting 70 nm thin sections by a cryo-ultramicrotome UCT (Leica, Vienna, Austria) operating at −100°C. Sections were collected on a 600-mesh copper grid. Cryogenic fracture surfaces of composite samples were observed at various magnifications by using a Zeiss Supra 40 (Berlin, Germany) field emission scanning electron microscope, at an acceleration voltage of 1.50 kV. Thin (70–80 μm) films required for the analysis of the glass fiber length distribution were obtained by a further hot pressing stage (temperature 200°C, pressure 4 MPa, time 10 min) on the composite plaques. Each film specimen was observed by an optical microscope (Leitz Ortholux II POL-BK) through a video camera (PIKE F032C). At least 200 measurements of glass fiber length were acquired in order to estimate the number and weight average fiber length.

Thermal characterization. Differential scanning calorimetry (DSC) tests were carried out by a Mettler® DSC30 apparatus (Schwerzenbach, Switzerland) under a constant nitrogen flow of 100 ml/min. The samples were heated up to 200°C at a rate of 10°C/min, followed by cooling at the same rate to 0°C. A second

heating scan was performed at 10°C/min. The melting enthalpy of 100% crystalline isotactic PP has been taken as $\Delta H^0 = 209$ J/g.[26] The crystallization enthalpy ΔH_c was measured by integrating the heat flow curve during the cooling scan. The crystallinity χ_c of the composite samples was calculated by taking the weight fraction of PP in the composite into account. Moreover, the melting temperatures T_{m1} and T_{m2} were recorded during the first and second heating scan, respectively.

Mechanical testing

Uniaxial ramp tensile tests were performed with an Instron model 4502 (Norwood, USA) tensile tester equipped with a 10 kN load cell, on samples consisting of at least five rectangular unnotched specimens of 27 mm × 120 mm × 2.7 mm. Tests were carried out at a crosshead speed of 0.25 mm/min up to a maximum axial deformation of 1%. The strain was recorded by using a resistance extensometer Instron® model 2620-601 with a gage length of 12.5 mm. As prescribed by ISO 527 standard, the elastic modulus was measured as a secant value between longitudinal deformation levels of 0.05 and 0.25%. Uniaxial ultimate mechanical properties such as stress (σ_b) and strain (ε_{br}) at break were determined at a higher crosshead speed (1 mm/min) without extensometer.

The plain-strain fracture toughness of the materials was characterized on some selected samples in terms of critical stress intensity factor (K_{Ic}) and the critical strain energy release rate (G_{Ic}). Three-point bending tests were performed with an Instron model 4502 (Norwood, USA) tensile tester equipped with a 10 kN load cell on single edge notched specimens with dimension of $5.4 \times 2.7 \times 23.8$ mm^3 (W x B x L) and nominal initial crack length (a_0) of 3.0 mm. Tests were carried out at a crosshead speed of 10 mm/min in according to the standard ASTM D5045.

Creep tests were performed by a dynamic mechanical analyzer (DMA) DMA Q800 (TA Instruments, New Castle, USA) applying a constant stress (σ_0) of 3 MPa for 3600 s at 30°C. Rectangular strips 25 mm long, 5 mm wide and 0.20 mm thick were tested, adopting a gauge length of 11.5 mm. The creep compliance D(t), computed as the ratio between the strain and the creep stress, was evaluated.

DMA was carried out with a DMA Q800 testing machine over a temperature range between –20 and 160°C, imposing a heating rate of 3°C/min and a frequency of 1 Hz. A preload of 0.2 MPa and a maximum strain of 0.05% was imposed on rectangular samples 25 mm long, 5 mm wide, and 0.20 mm thick. The most important viscoelastic functions (E', E'', $tan\delta$) were recorded at various temperatures.

Tensile impact tests were carried out with a CEAST® (Norwood, USA) tensile impact instrumented pendulum. The striker, with a mass of 3.65 kg and an initial angular position of 130°, had an impact speed of 3.5 m/s and a total impact energy of about 22 J. The specific tensile energy to break (TEB), obtained by integrating load–displacement curves, was obtained by applying equation (1)

$$TEB = \frac{1}{A}\left[V_0 \int_0^{tr} F\,dt - \frac{1}{2m}\left[\int_0^{tr} F\,dt\right]^2\right] \qquad (1)$$

where A is the cross section of the specimen, m is the striker mass, and V_0 is the impact speed.

Results and discussion

Microstructure

TEM analyses allow an estimation of the nanofiller distribution and also of the agglomerates dimension. In particular, from TEM micrographs of PP-silica samples it can be seen that silica agglomerates appear distributed quite inhomogeneously within the matrix in both samples (Figure 1(a) and (c)), while the agglomerate dispersion and distribution improve upon incorporation of PPgMA (Figure 1(b) and (d)). Moreover, if compared with the corresponding nanocomposites prepared without the addition of PPgMA, the size of silica agglomerates in ternary nanocomposites is markedly lower. TEM micrographs of the PP-graphite nanocomposites show that graphite sheets are homogeneously dispersed in the compatibilized matrix (PP-PPgMA-5-xGnP-5) with an average dimension ranging from 100 to 300 nm (Figure 1(e)). On the other hand, it is observed that there are still some graphite sheets consisting of micrometer particles in the uncompatibilized matrix (Figure 1(f)). X-ray diffraction (XRD) analyses were used to study the crystalline structure of the PP-graphite nanocomposites and the results were reported in one of our previous work.[17] In particular, it was observed that the interplanar distance between graphene layers does not change significantly in PP nanocomposites, as determined by applying the Bragg's law. Moreover, the graphite crystal size, as computed by applying the Scherer's equation, was found to increase appreciably with the graphite content indicating that some sheets are agglomerating during the compounding of the nanocomposites. On the other hand, the sample PP-PPgMA-5-xGnP-5 showed a smaller crystal size than the sample PP-xGnP-5, evidencing that xGnP is better dispersed due to the incorporation of compatibilizer PPgMA, thus corroborating the indications coming from TEM observations.

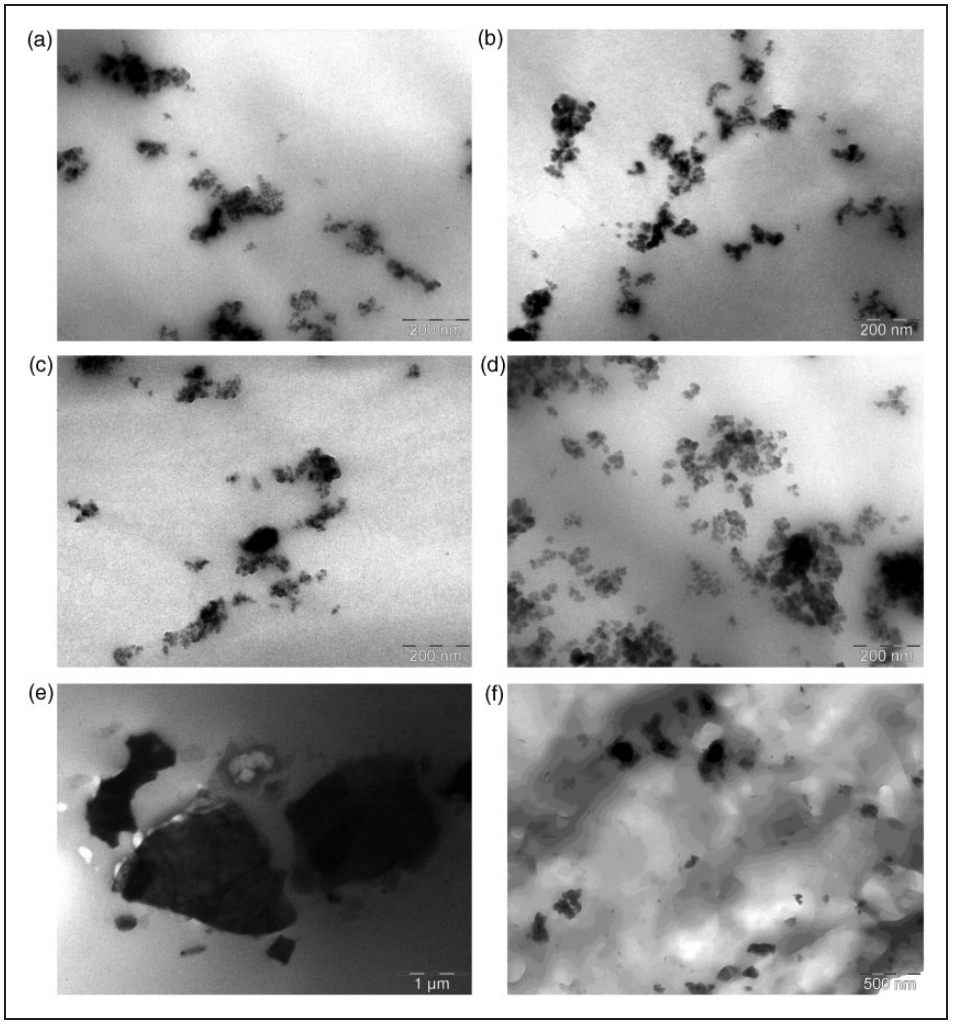

Figure 1. TEM micrographs of cryocut surfaces of (a) PP-A380-5, (b) PP-PPgMA-5-A380-5, (c) PP-R974-5, (d) PP-PPgMA-5-R974-5, (e) PP-xGnP-5 and (f) PP-PPgMA-5-xGnP-5.

Scanning electron microscopy (SEM) images of fracture surfaces for PP nanocomposites loaded with 10 wt% of SGF are shown in Figure 2. The glass fibers are generally well dispersed in the unfilled PP matrix, and several fibers result to be pulled out from the matrix (Figure 2(a)). In fact, interfacial debonding appears to be the dominant failure mechanism which is generally associated to a poor fiber–matrix adhesion (Figure 2(d)). On the other hand, Figure 2(b) indicates a quite different failure behavior for composites containing a compatibilizer (PPgMA). In this case, the length of the protruding fibers is significantly lower and SGF seems to be more efficiently wetted by the polymer matrix (Figure 2(e)). Composites based on ternary PP matrices (i.e. PP-PPgMA-5-A380-5/GF-10, PP-PPgMA-5-R974-5/GF-10, and PP-PPgMA-5-xGnP-5/GF-10) showed a qualitatively homogeneous dispersion of SGF and a shorter length of the protruding fibers. Similar considerations can be drawn for the composites based on binary PP matrices additivated with xGnP (Figure 2(c) and (f)). The above experimental observations are in good agreement with the results obtained for fiber–matrix ISS from micromechanical tests on microcomposites with the same composition.[16,17] Fiber length plays an important effect on the mechanical properties of short fiber reinforced composites, and glass fibers can be fractured in melt processing steps.[27] According to the theory of Kelly and Tyson,[28] the minimum fiber length that allows the ultimate strength of the fiber to be reached is called the critical fiber length, L_c, and is given by

$$\frac{L_c}{\bar{d}} = \frac{\sigma_{fb(Lc)}}{2 \cdot ISS} \tag{2}$$

where $\bar{d}$ is the average glass fiber diameter ($15.3 \pm 1.5\,\mu m$), $\sigma_{fb(Lc)}$ is the ultimate fiber strength of a fiber with length L_c, and ISS is the fiber–matrix ISS.

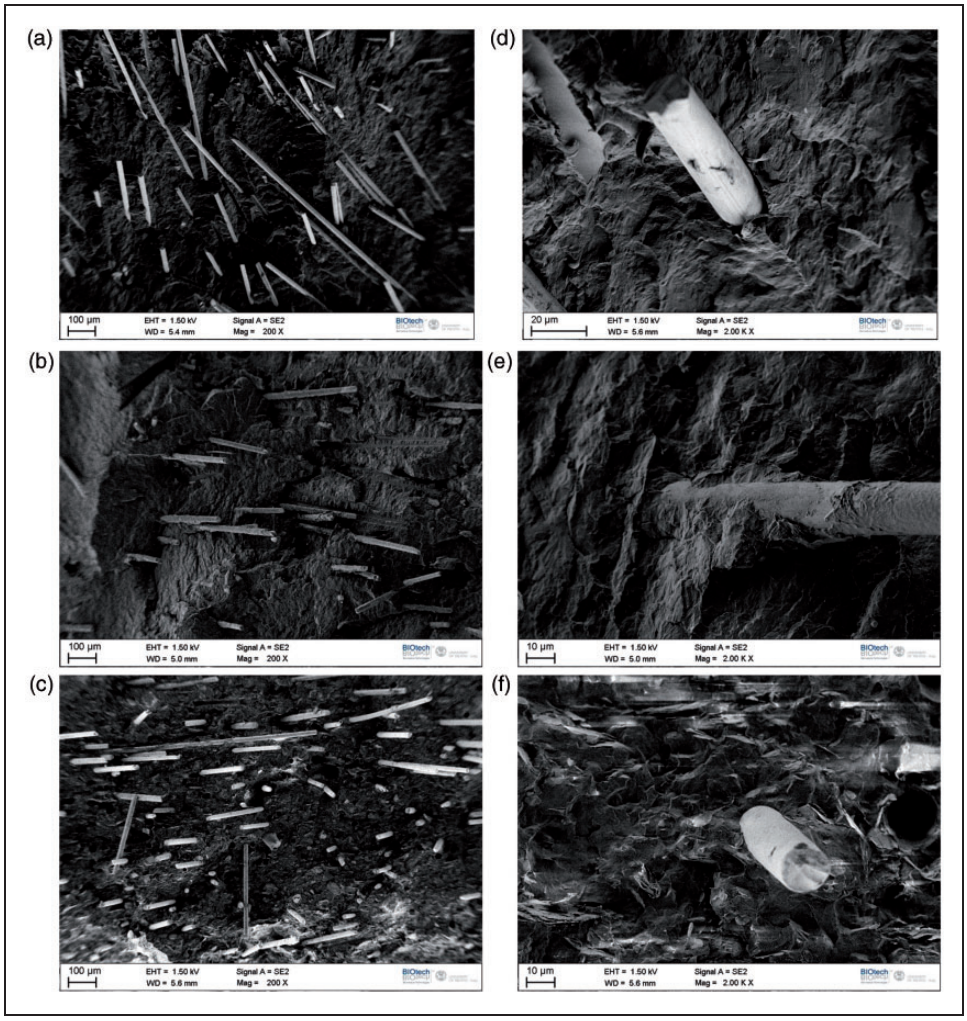

Figure 2. SEM micrographs of fractured surfaces of SGF reinforced nanocomposites: (a,d) PP/GF-10, (b,e) PP-PPgMA-10/GF-10, and (c,f) PP-xGnP-7/GF-10.

In particular, L_c was experimentally measured in model composites through SFFT and ISS was computed in according to the Kelly–Tyson approach.[16,17] Since L_c is significantly larger than the average fiber lengths determined from image analysis for PP/GF composites, as it will be presented later, many glass fibers are expected to be pulled out instead of fracturing during loading of the composite. On the other hand, average fiber lengths are comparable to L_c values for the GF composites based on PP-PPgMA-10 matrix and GF composites based on ternary matrices (i.e. PP-PPgMA-5-A380-5/GF-10, PP-PPgMA-5-R974-5/GF-10, and PP-PPgMA-5-xGnP-5/GF-10) (Table 1). Average fiber lengths are generally higher than L_c values in the case of GF composites based on binary matrices PP-xGnP.

The measurement of fiber length distribution was carried out by image analysis on the films of composite samples through optical microscopy. A number ($\overline{L_n}$) and a weight ($\overline{L_w}$) average fiber length are calculated by equations (3) and (4), respectively

$$\overline{L_n} = \frac{\sum n_i L_i}{\sum n_i} \tag{3}$$

$$\overline{L_w} = \frac{\sum n_i L_i^2}{\sum n_i L_i} \tag{4}$$

where n_i is the number of SGF within a specified range around the length value L_i. The number and the weight aspect ratios between the average glass fiber length and the mean fiber diameter are computed as $\overline{R_n} = \overline{L_n}/\bar{d}$ and $\overline{R_w} = \overline{L_w}/\bar{d}$, respectively. $\overline{R_n}$ values are reported in Figure 3(a) for various types of hybrid composites as a function of the SGF content. For all composites, there is a substantial decrease in the average aspect ratio of the glass fiber as its content increases.

Table 1. Average lengths and aspect ratios of SGF as measured in the composites.

Sample	$\overline{L_n}$ (mm)	$\overline{L_w}$ (mm)	$\overline{L_c}$ (mm)	$\overline{R_n}$	$\overline{R_w}$
PP/GF-5	0.87	0.89	5.96 ± 0.41	56.7	58.6
PP/GF-10	0.71	0.82		46.6	53.9
PP/GF-20	0.53	0.60		34.9	39.3
PP-PPgMA-10/GF-5	1.11	1.20	1.29 ± 0.48	72.3	78.5
PP-PPgMA-10/GF-10	1.03	1.09		67.1	71.4
PP-PPgMA-10/GF-20	0.69	0.75		45.4	49.2
PP-PPgMA-5-A380-5/GF-5	0.88	0.98	1.24 ± 0.25	57.3	63.8
PP-PPgMA-5-A380-5/GF-10	0.80	0.85		52.3	55.6
PP-PPgMA-5-A380-5/GF-20	0.61	0.66		39.8	43.1
PP-PPgMA-5-R974-5/GF-5	0.84	0.86	0.77 ± 0.07	54.9	56.3
PP-PPgMA-5 - R974-5/GF-10	0.79	0.84		51.9	54.6
PP-PPgMA-5 - R974-5/GF-20	0.66	0.69		43.4	45.2
PP-PPgMA-5-xGnP-5/GF-5	0.82	0.84	0.79 ± 0.12	53.4	54.9
PP-PPgMA-5-xGnP-5/GF-10	0.69	0.71		45.0	46.7
PP-PPgMA-5-xGnP-5/GF-20	0.60	0.62		39.4	40.3
PP-xGnP-1/GF-10	0.84	0.85	2.99 ± 0.39	46.1	53.5
PP-xGnP-3/GF-10	0.78	0.80	1.95 ± 0.31	45.8	52.5
PP-xGnP-5/GF-10	0.68	0.69	1.60 ± 0.15	44.3	45.2
PP-xGnP-7/GF-10	0.65	0.66	1.52 ± 0.26	42.6	43.3

$\overline{L_n}$: number average fiber length, equation (3).
$\overline{L_w}$: weight average fiber length, equation (4).
$\overline{L_c}$: critical average fiber length, as measured by the fragmentation test on model composites.[16,17]
$\overline{R_n}$: number average fiber aspect ratio, i.e. $\overline{L_n}/d$ where d is the average glass fiber diameter (15.3 ± 1.5 μm).
$\overline{R_w}$: weight average fiber aspect ratio, i.e. $\overline{L_w}/d$.

Fiber breakage may result from fiber–polymer interaction, fiber–fiber interaction (due to bending stresses caused by fiber overlap and stress concentrations caused by fiber surface abrasion), and fiber contact with surfaces of the processing equipment.[29] It is noteworthy that when xGnP is added to systems a pronounced reduction of the SGF aspect ratio can be observed (Figure 3(b)). This effect can be attributed to the matrix viscosity increase due to xGnP introduction and the resulting higher shear stresses in the system. Moreover, as already documented by Yoo et al. for nylon 6–glass composites modified with organoclay particles,[27] the particle impingement during melt processing can be another reason for an increased attrition with glass fiber and this has increased importance at high filler concentrations.

Mechanical testing

As the amount of SGF increases, both tensile modulus and strength increase, while the elongation at break decreases (Table 2). This behavior is quite peculiar for short fiber reinforced polymer composites.[1] It is interesting to observe that the presence of the PPgMA compatibilizer does not modify the mechanical properties of the unfilled polymer matrix, but slightly improves those of the SGF filled composites. This result can certainly be attributed to the positive effect on the fiber/matrix interface. Similar effects can be observed when 5 wt% of nanofillers A380, R974, and xGnP are added.

From the results obtained by DSC measurements (Table 2), it can be seen that the glass fibers content do not appreciably affect the melting temperature and degree of crystallinity of the composites. On the other hand, the crystallization peak temperature, T_c, is slightly increased in SGF composites with respect to neat nanocomposite matrices, probably due to the nucleating effect of SGF.[30]

There have been numerous attempts to model the elastic modulus of micro- and nanocomposites and to correlate the experimental data with composite models.[7,9,31] In particular, Halpin–Tsai and Mori–Tanaka theories have been widely applied to predict the tensile modulus of short fiber composites. Both theories are generally used as models for a single-filler population in a matrix. However, the composites studied in the present work consist of both a nanofiller

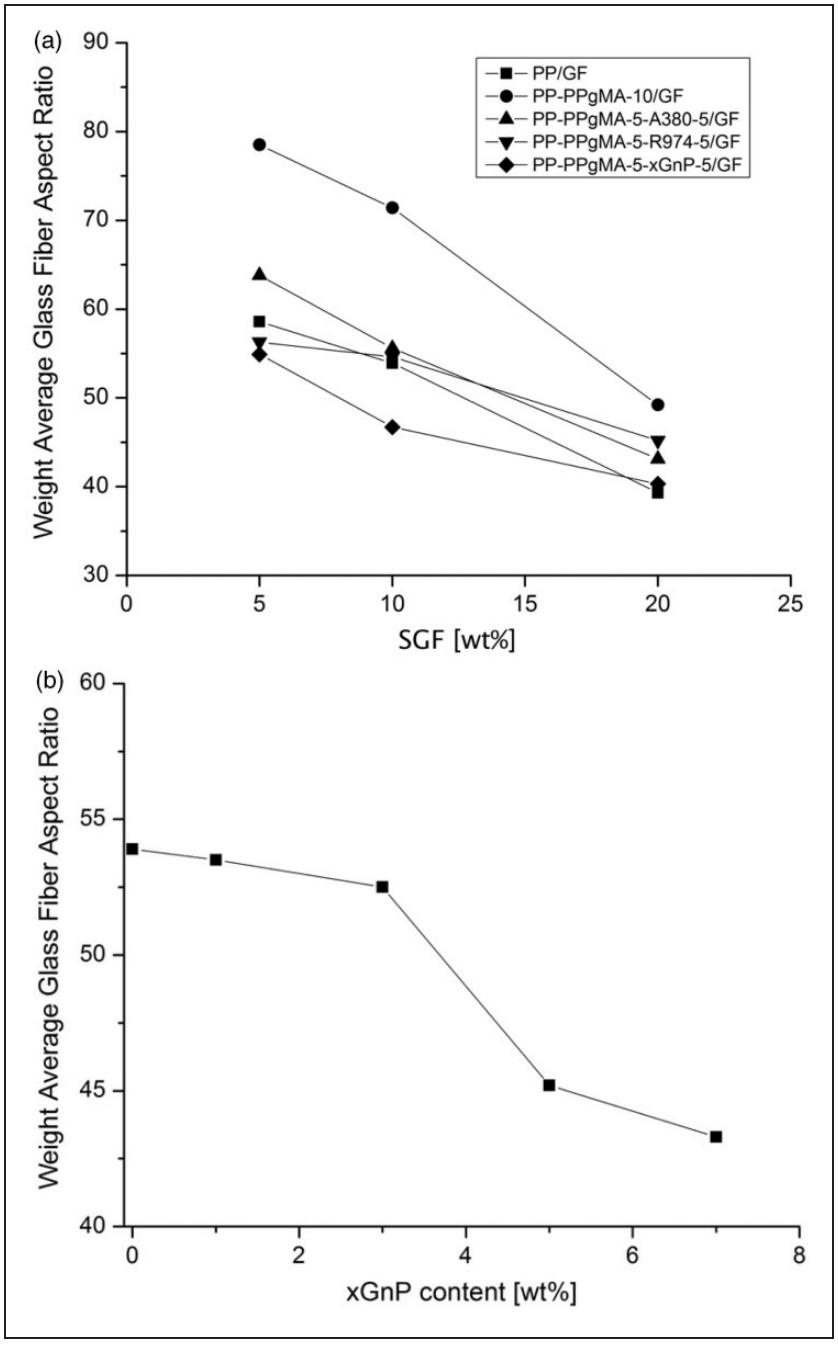

Figure 3. (a) Weight average glass fiber aspect ratio as a function of (a) SGF content for binary and ternary composites and (b) xGnP content for composites loaded with 10 wt% of SGF.

(silica or expanded graphite) and a microfiller (glass fibers). Recently, Spencer et al.[32] proposed a two-population approach to model the combined effect of exfoliated montmorillonite (nanofillller) and intercalated tactoids (microfiller), while Yoo et al.[27] applied a similar approach to consider the effects of both organoclay and SGFs. If the tensile modulus is considered, a two-population model can be developed in terms of an additive approach (equation (5)) or a multiplicative approach (equation (6))

$$\frac{E_{add}}{E_m} = \frac{E_{GF}}{E_m} + \frac{E_{nc}}{E_m} - 1 \tag{5}$$

$$\frac{E_{mult}}{E_m} = \frac{E_{nc}}{E_m} \cdot \frac{E_{GF}}{E_{nc}} \tag{6}$$

Table 2. Tensile mechanical properties and thermal properties of the composite samples.

Sample	E (MPa)	σ_b (MPa)	ε_{br} (%)	ISS (MPa)	TEB (J/mm^2)	K_{Ic} (MPa m$^{1/2}$) (G_{Ic} (kJ/m^2))	T_c (°C)	χ_c (%)	$T_{m,2}$ (°C)
(PP)	1546 ± 24	37.1 ± 0.1	16.8 ± 0.3	2.7 ± 0.2	0.19 ± 0.05		115.6	48.8	165.10
PP/GF-5	2086 ± 42	39.3 ± 0.3	6.2 ± 0.5				115.3	48.0	164.7
PP/GF-10	2896 ± 53	42.1 ± 0.5	3.6 ± 0.4		0.43 ± 0.06	3.1 ± 0.1 (2.8 ± 0.1)	117.1	48.8	165.7
PP/GF-20	3697 ± 41	46.6 ± 0.7	2.8 ± 0.6				116.6	48.6	165.2
(PP-PPgMA-10)	1648 ± 12	37.0 ± 0.5	12.1 ± 0.6	20.2 ± 2.5	0.25 ± 0.02		117.9	48.0	162.8
PP-PPgMA-10/GF-5	2595 ± 63	40.6 ± 0.4	5.8 ± 0.5				117.8	46.9	163.8
PP-PPgMA-10/GF-10	3035 ± 51	43.2 ± 0.6	3.4 ± 0.6		0.51 ± 0.06	3.3 ± 0.1 (3.2 ± 0.1)	119.3	46.7	163.1
PP-PPgMA-10/GF-20	3859 ± 66	48.0 ± 0.7	2.5 ± 0.8				117.5	48.7	164.5
(PP-PPgMA-5-A380-5)	2015 ± 40	35.7 ± 0.4	6.7 ± 0.2	22.7 ± 2.1	0.24 ± 0.06		117.5	49.4	166.0
PP-PPgMA-5-A380-5/GF-5	2614 ± 37	39.4 ± 0.4	5.6 ± 0.5				116.2	48.0	166.6
PP-PPgMA-5-A380-5/GF-10	3302 ± 48	43.0 ± 0.6	3.3 ± 0.6		0.49 ± 0.09	3.5 ± 0.1 (3.3 ± 0.2)	115.8	48.6	166.8
PP-PPgMA-5-A380-5/GF-20	4042 ± 44	47.8 ± 0.8	2.4 ± 0.7				116.2	49.6	166.6
(PP-PPgMA-5-R974-5)	2281 ± 58	34.2 ± 0.4	12.0 ± 1.1	38.8 ± 3.5	0.28 ± 0.04		115.3	50.8	166.7
PP-PPgMA-5-R974-5/GF-5	2862 ± 48	39.2 ± 0.6	5.4 ± 0.6				119.5	48.1	164.2
PP-PPgMA-5 - R974-5/GF-10	3402 ± 52	43.4 ± 0.5	3.2 ± 0.6		0.54 ± 0.04	3.7 ± 0.2 (3.5 ± 0.2)	120.0	49.1	164.0
PP-PPgMA-5 - R974-5/GF-20	4171 ± 40	48.2 ± 0.7	2.2 ± 0.7				118.9	49.2	164.5
(PP-PPgMA-5-xGnP-5)	3058 ± 114	34.3 ± 0.3	7.1 ± 1.0	39.0 ± 5.7	0.31 ± 0.05		122.3	50.4	165.7
PP-PPgMA-5-xGnP-5/GF-5	3612 ± 55	39.5 ± 0.5	5.0 ± 0.7				124.2	47.8	166.5
PP-PPgMA-5-xGnP-5/GF-10	4012 ± 61	44.1 ± 0.5	2.5 ± 0.6		0.52 ± 0.07	3.9 ± 0.1 (3.6 ± 0.2)	124.7	47.9	165.9
PP-PPgMA-5-xGnP-5/GF-20	4758 ± 49	48.6 ± 0.7	2.0 ± 0.6				127.1	48.6	164.0
PP-xGnP-1/GF-10	3224 ± 52	43.5 ± 0.5	3.0 ± 0.5	6.7 ± 0.9	0.40 ± 0.06	3.1 ± 0.1 (2.8 ± 0.1)	124.0	48.5	165.7
PP-xGnP-3/GF-10	3542 ± 55	43.8 ± 0.6	2.9 ± 0.5	11.8 ± 1.2	0.44 ± 0.09	3.2 ± 0.1 (2.9 ± 0.1)	124.2	48.9	167.0
PP-xGnP-5/GF-10	3834 ± 43	44.0 ± 0.5	2.5 ± 0.5	15.3 ± 1.3	0.38 ± 0.07	3.2 ± 0.1 (3.0 ± 0.2)	124.6	47.7	166.0
PP-xGnP-7/GF-10	3959 ± 61	44.3 ± 0.6	2.3 ± 0.6	16.4 ± 1.8	0.33 ± 0.05	3.3 ± 0.1 (3.2 ± 0.2)	124.7	48.0	166.5

E: tensile modulus; G_{Ic}: critical strain energy release rate; $ISS_{K\text{-}T}$: interfacial shear strength[16,17]; K_{Ic}: critical stress intensity factor; T_c: crystallization peak temperature; TEB: specific tensile energy at break; $T_{m,2}$: melting temperature (second scan); ε_{br}: tensile strain at break; σ_y: tensile stress at break; χ_c: normalized crystallinity.

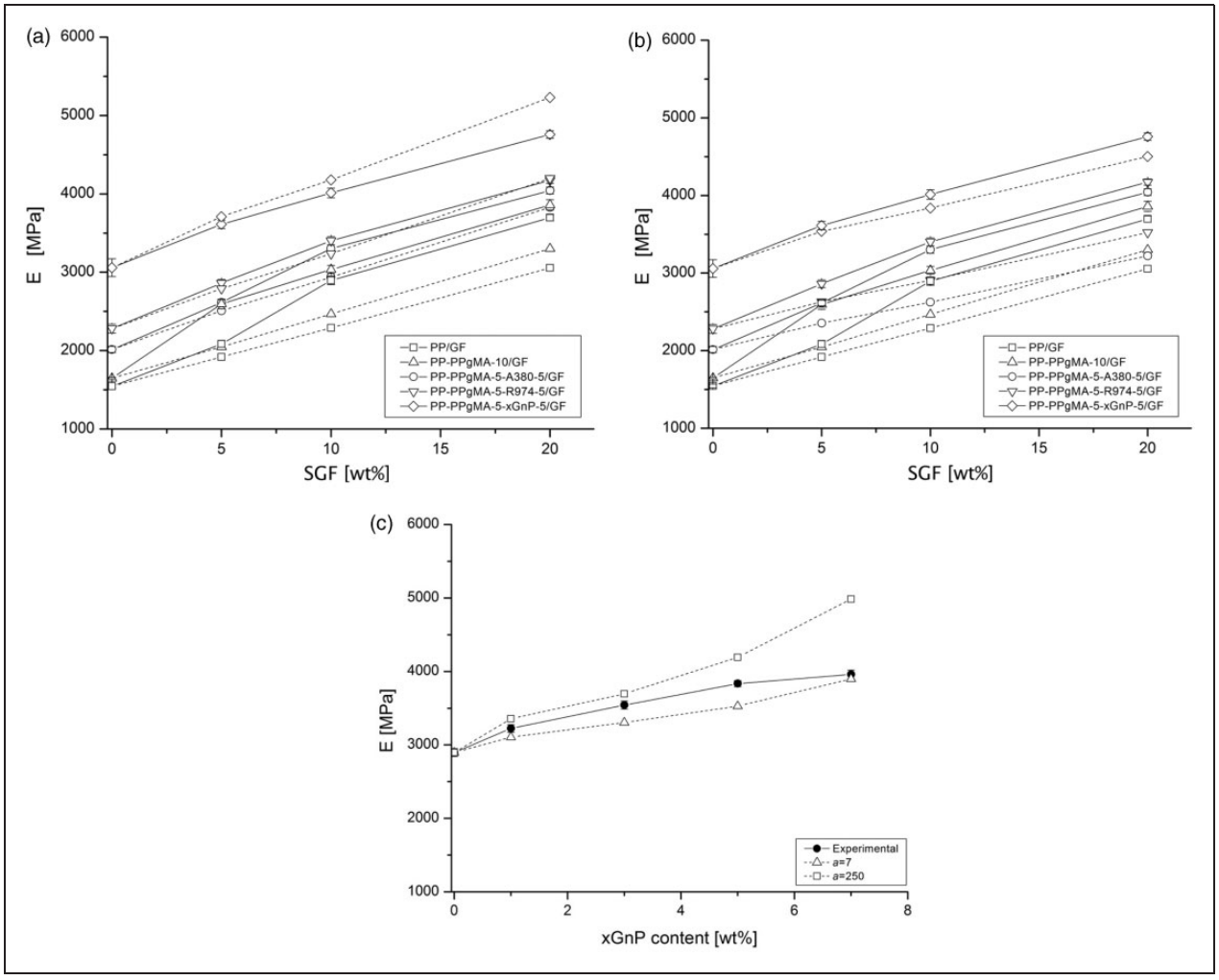

Figure 4. Comparison between elastic modulus predictions (dashed lines) and experimental values (solid lines). Predictions are based on the additive two-population model, for SGF reinforced composites containing (a) 0–20 wt% GF, applying the Halpin–Tsai and Tsai–Pagano theory, (b) 0–20 wt% of SGF, adopting the Halpin–Tsai and Christensen–Waals models, (c) 10 wt% of SGF and 0–7 wt% xGnP applying the Halpin–Tsai and Tsai–Pagano theory.

here E_{GF} and E_{nc} are the moduli of the composites based on the glass fibers and on the nanofiller, respectively, whereas E_m is the modulus of the neat matrix. While in the additive approach the contributions of each filler are calculated separately and summed together without double counting the matrix contribution, in the multiplicative approach the contribution of the nanofiller is calculated first and the nanocomposite is then considered to be the matrix for the glass fiber reinforcement. Both methods predict similar stiffening effects, although the multiplicative approach gives slightly higher modulus values, as this model treats the nanocomposite as a matrix for the glass fiber reinforcement. The Halpin–Tsai theory (equations (7) and (8)) was employed to predict the tensile modulus of the nanocomposites

$$\frac{E_{nc}}{E_m} = \frac{1 + \xi\eta\varphi}{1 - \eta\varphi} \tag{7}$$

$$\eta = \frac{\frac{E_{nf}}{E_m} - 1}{\frac{E_{nf}}{E_m} + \xi} \tag{8}$$

here E_{nf} is the elastic modulus of the nanofiller, ξ is a geometrical correction factor (function of fillers' orientation and aspect ratio), and φ is the filler volume fraction. In particular, the factor ξ is assumed as $2\,a$ and $2/3\,a$ for nanosilica (i.e. spherical particles) and the xGnP

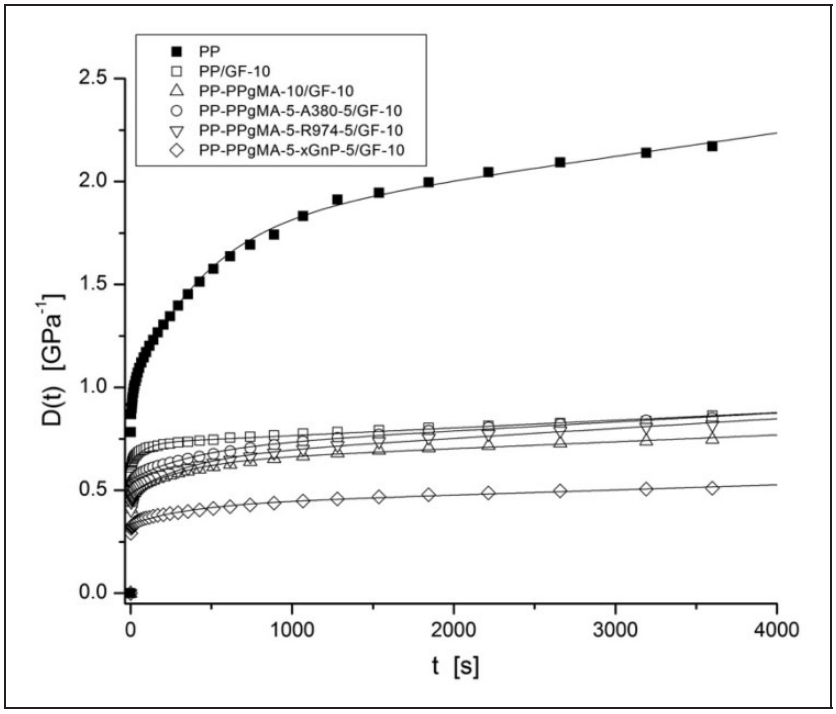

Figure 5. Creep compliance of composites loaded with 10 wt% of SGF (experimental data are fitted by the Burger's model[37,38]).

(platy particles), respectively, according to the Halpin–Tsai theory. The filler aspect ratio (a) of silica and xGnP fillers was considered as 1 (i.e. spherical particles) and 7,[17] respectively. Moreover, while E_f was assumed as 70 GPa for both silica[9] and xGnP.[33] This model accounts for the mechanical properties of components and fillers' geometry and aspect ratio, but assumes perfect adhesion at the polymer/filler interface, homogeneous dispersion, and specific filler orientation.[33] The main limitation of this model is that it does not account for filler agglomeration and the presence and properties of the interphase. Moreover, the Halpin–Tsai model assumes unidirectional alignment of the filler along the direction of the applied tensile load and it seems thus inappropriate for the short glass fiber composites under investigation. Therefore, a more appropriate empirical model proposed by Tsai and Pagano[34] was applied to predict the elastic modulus ($E_{GF,TP}$) of composites containing short fibers randomly oriented in a plane (equations (9) to (11)). Furthermore, since the short fibers are supposed to be randomly oriented throughout all the composite volume, the Christensen and Waals model[35,36] was used to estimate the elastic modulus ($E_{GF,CW}$) in three-dimensional randomly distributed short fiber composites (equation (12))

$$E_{GF,TP} = \frac{3}{8}E_{LL} + \frac{5}{8}E_{TT} \tag{9}$$

$$\frac{E_{LL}}{E_m} = \frac{1 + \xi_L \eta_L \varphi_f}{1 - \eta_L \varphi_f} \tag{10a}$$

$$\eta_L = \frac{\frac{E_f}{E_m} - 1}{\frac{E_f}{E_m} + \xi_L} \tag{10b}$$

$$\frac{E_{TT}}{E_m} = \frac{1 + \xi_T \eta_T \varphi_f}{1 - \eta_T \varphi_f} \tag{11a}$$

$$\eta_T = \frac{\frac{E_f}{E_m} - 1}{\frac{E_f}{E_m} + \xi_T} \tag{11b}$$

where the subscripts L and T stand for longitudinal and transversal, while ξ_L and ξ_T is assumed as $2a$ and 2, respectively, according to the Tsai and Pagano's theory

$$E_{GF,CW} = \frac{\varphi_f}{6}E_f + \left[1 + (1 + \nu_m)\varphi_f\right]E_m \tag{12}$$

where E_f is the elastic modulus of the glass fibers, φ_f is the fiber volume content, while ν_m is Poisson's ratio of the matrix. In the case of SGF composites the aspect ratio (a) was experimentally measured on each sample. Finally, as experimentally determined in a previous work, a value E_f of 63 GPa was considered for E-glass fibers,[16] while ν_m was experimentally determined as 0.46 ± 0.01.

Table 3. Viscoelastic properties of GF composites.

Sample	E'_{25C}(MPa)	E''_{25C}(MPa)	$\tan\delta_{25^\circ C}$	D_{3600s}(GPa^{-1})
(PP)	2006.2	88.9	4.43	2.17
PP/GF-5	2244.0	95.4	4.25	1.22
PP/GF-10	2305.1	97.0	4.21	0.86
PP/GF-20	3143.9	116.0	3.69	0.74
(PP-PPgMA-10)	1353.2	70.1	5.18	2.05
PP-PPgMA-10/GF-5	2233.5	97.4	4.36	0.99
PP-PPgMA-10/GF-10	2339.1	100.1	4.28	0.75
PP-PPgMA-10/GF-20	3176.4	132.1	4.16	0.62
(PP-PPgMA-5-A380-5)	2669.4	133.5	5.00	1.64
PP-PPgMA-5-A380-5/GF-5	3009.5	145.1	4.82	0.90
PP-PPgMA-5-A380-5/GF-10	3155.9	150.5	4.77	0.85
PP-PPgMA-5-A380-5/GF-20	3891.7	183.3	4.71	0.64
(PP-PPgMA-5-R974-5)	2646.6	114.7	4.34	1.81
PP-PPgMA-5-R974-5/GF-5	2691.0	115.4	4.29	1.00
PP-PPgMA-5 - R974-5/GF-10	2959.5	123.7	4.18	0.82
PP-PPgMA-5 - R974-5/GF-20	4176.2	159.1	3.81	0.68
(PP-PPgMA-5-xGnP-5)	2277.4	100.7	4.42	0.98
PP-PPgMA-5-xGnP-5/GF-5	3359.6	146.5	4.36	0.77
PP-PPgMA-5-xGnP-5/GF-10	3828.6	166.2	4.34	0.51
PP-PPgMA-5-xGnP-5/GF-20	4513.7	194.1	4.30	0.46
PP-xGnP-1/GF-10	2978.9	124.5	4.18	0.82
PP-xGnP-3/GF-10	3287.9	136.1	4.14	0.76
PP-xGnP-5/GF-10	3550.9	148.1	4.17	0.70
PP-xGnP-7/GF-10	3933.3	161.7	4.11	0.63

D_{3600s}: viscoelastic creep compliance at 3600 s; E'_{25C}: storage modulus at +25°C; E''_{25C}: loss modulus at +25°C; $\tan\delta_{25^\circ C}$: loss tangent at +25°C.

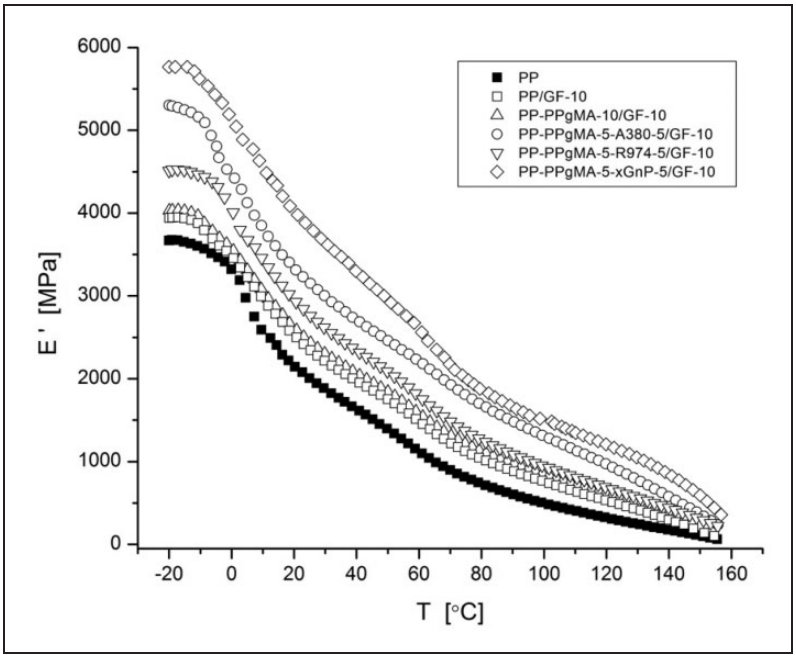

Figure 6. Storage modulus (*E'*) of composites loaded with 10 wt% of SGF.

The elastic modulus predictions for SGF reinforced PP nanocomposites as a function of SGF content, using the additive two-population method, are presented in Figure 4(a). Individual contributes of nanofiller and SGF were considered by applying the Halpin–Tsai and the Tsai–Pagano models, respectively. The model predicts quite well the modulus for composite samples based on nanocomposite matrix, with a slight overestimation for SGF content higher than 10 wt%, probably due to differences in assumed and actual filler aspect ratio and orientation.[27] Moreover, the predicted modulus values are generally lower for the samples PP/GF and PP-PPgMA-10/GF. On the other hand, predicted values of modulus obtained by applying the Christensen and Waals model were considerably lower than the experimental values (Figure 4(b)). The model predictions for SGF composites as a function of xGnP amount according to Halpin–Tsai and the Tsai–Pagano models are shown in Figure 4(c). In particular, experimental data were compared to theoretical values in two different cases: (i) aspect ratio of 250 on the basis of the supplier information ($a = 250$) and (ii) aspect ratio of 7 on the basis of the morphological analysis ($a = 7$) which accounts for agglomeration. The Tsai–Pagano model overpredicts the modulus when the aspect ratio of 250 is used, indicating that agglomeration occurred and a reduced aspect ratio needs to be considered. On the other hand, when an aspect ratio of 7 is considered, the model slightly underpredicts the modulus, accounting for agglomeration but neglecting the presence of the interphase.[33] The effect of filler type on reinforcement can be seen by comparing Figure 4(a) and (c). Interesting, the improvement in tensile modulus by xGnP incorporation is similar to that obtained by SGF at low filler contents (0–10 wt%), probably due to the similar values in modulus and aspect ratio of the micro- (GF) and nano- (xGnP) fillers.

The toughness of the composites, evaluated through the critical stress intensity factor (K_{IC}) and strain energy release rate (G_{IC}), improved when SGFs are incorporated. Moreover, superior resistance to crack initiation was recorded with increasing amounts of xGnP.

Interestingly, TEB values increased with glass fiber incorporation but slightly decreased with increased xGnP content, probably due to diffuse filler aggregation and agglomeration which produced a considerable decrease in strength. The observed increase in absorbed impact energy reflects the increased stiffness and strength of the composites that overshadows the loss in ductility, resulting in a larger area under the force–deflection curve (Table 2).

The effect of the incorporation of SGF on the creep resistance of PP nanocomposite matrices is reported in Figure 5. As the SGF content increases, the creep compliance is strongly reduced, showing a remarkable improvement of the creep stability of PP nanocomposites induced by the presence of rigid fibers (Table 3). Interestingly, the sample PP-PPgMA-10/GF-10 manifested better creep stability than PP/GF-10, probably due to the substantial better interfacial properties rather than the slightly higher stiffness. On the other hand, the best creep performances are exhibited by the composite PP-PPgMA-5-xGnP-5/GF-10 which showed highest stiffness and *ISS*.

The dynamic mechanical properties of the composites under investigation are significantly influenced by the fiber weight fraction: as expected, both storage (E') and loss (E'') modulus increase with higher GF contents (Figure 6), while the loss tangent decreases (Table 3). Concurrently, the incorporation of xGnP in composites loaded with 10 wt% GF produces a substantial increase of E' and E'' and a slight decrease of the loss tangent with the filler content, showing that the elasticity of the composite is improved by the addition of expanded graphite.

Conclusions

The structure and property relationships of SGF reinforced PP nanocomposites prepared by melt compounding and compression molding have been investigated to explore the combined reinforcing effect given from two fillers of very different size scales (micro- and nano-scale). After processing, a reduction in glass fiber length was observed as fiber loading increased, with a significant further reduction as nanofillers were added. The tensile modulus and strength of the composites increased, while the elongation at break decreased as the content of SGF increased. Further improvements in modulus and strength were observed in hybrid composites incorporating both SGF and the nanofiller. Addition of a small amount of nanofiller resulted in a greater adhesion between fiber and matrix, as confirmed by morphological observations, leading to a better stress transfer at the fiber–matrix interface. A two-population model, based on the Halpin–Tsai and Tsai–Pagano theories, was used to predict the elastic modulus of the hybrid composites. Comparison with the experimental results indicates that the model can satisfactory predict the modulus of the composites when the aspect ratio of the nanofiller is taken into account.

The stronger interfacial strength exhibited in hybrid composites positively affected the viscoelastic behavior of the materials, leading to higher storage modulus and enhanced creep stability. In conclusion, the results indicate that hybrid composites combining the advantages of nanofillers and micro-size reinforcements can be successfully produced in order to obtain lighter and

stronger materials, as part of the higher density SGF can be replaced with a smaller amount of nanofiller.

Conflict of interest

None declared.

Funding

This research received no specific grant from any funding agency in the public, commercial, or not-for-profit sectors.

References

1. Wetherhold RC. Short-fiber-reinforced polymeric composites: Structure–property relations. In: Nicolais L and Borzacchiello A (eds) *Wiley encyclopedia of composites*, 2nd ed. Hoboken, NJ: John Wiley & Sons, 2012.
2. Karger-Kocsis J. Polypropylene: An A-Z reference. Dordrecht, The Netherlands: Kluwer Publishers, 1999.
3. Pegoretti A and Ricco T. Fatigue crack propagation in polypropylene reinforced with short glass fibres. *Compos Sci Technol* 1999; 59: 1055–1062.
4. Pedrazzoli D, Dorigato A and Pegoretti A. Monitoring the mechanical behaviour of electrically conductive polymer nanocomposites under ramp and creep conditions. *J Nanosci Nanotechnol* 2012; 12: 4093–4102.
5. Tait M, Pegoretti A, Dorigato A, et al. The effect of filler type and content and the manufacturing process on the performance of multifunctional carbon/poly-lactide composites. *Carbon* 2011; 49: 4280–4290.
6. Dorigato A, Sebastiani M, Pegoretti A, et al. Effect of silica nanoparticles on the mechanical performances of poly(lactic acid). *J Polym Environ* 2012; 20: 713–725.
7. Dorigato A, Dzenis Y and Pegoretti A. Filler aggregation as a reinforcement mechanism in polymer nanocomposites. *Mech Mater* 2013; 61: 79–90.
8. Dorigato A, Pegoretti A and Kolařík J. Nonlinear tensile creep of linear low density polyethylene/fumed silica nanocomposites: Time-strain superposition and creep prediction. *Polym Compos* 2010; 31: 1947–1955.
9. Dorigato A, Dzenis Y and Pegoretti A. Nanofiller aggregation as reinforcing mechanism in nanocomposites. *Proc Eng* 2011; 10: 894–899.
10. Hussain F. Review article: Polymer-matrix nanocomposites, processing, manufacturing, and application: An overview. *J Compos Mater* 2006; 40: 1511–1575.
11. Ramsaroop A. Fracture toughness studies of polypropylene-clay nanocomposites and glass fibre reinforced polypropylene composites. *Mater Sci Appl* 2010; 01: 301–309.
12. Rybiński P, Janowska G, Jóźwiak M, et al. Thermal stability and flammability of butadiene–styrene rubber nanocomposites. *J Therm Anal Calorim* 2012; 109: 561–571.
13. Du M, Guo B and Jia D. Thermal stability and flame retardant effects of halloysite nanotubes on poly(propylene). *Eur Polym J* 2006; 42: 1362–1369.
14. Dorigato A, Pegoretti A and Frache A. Thermal stability of high density polyethylene–fumed silica nanocomposites. *J Therm Anal Calorim* 2012; 109: 863–873.
15. Gibson RF. A review of recent research on mechanics of multifunctional composite materials and structures. *Compos Struct* 2010; 92: 2793–2810.
16. Pedrazzoli D and Pegoretti A. Silica nanoparticles as coupling agents for polypropylene/glass composites. *Compos Sci Technol* 2013; 76: 77–83.
17. Pedrazzoli D and Pegoretti A. Expanded graphite nanoplatelets as adhesion promoters in glass fiber reinforced polypropylene composites. *Compos Part A Appl Sci Manuf* in press.
18. Kalaitzidou K, Fukushima H and Drzal LT. Multifunctional polypropylene composites produced by incorporation of exfoliated graphite nanoplatelets. *Carbon* 2007; 45: 1446–1452.
19. Chamis CC. Polymer composite mechanics review 1965 to 2006. *J Reinf Plast Compos* 2007; 26: 987–1019.
20. Dorigato A and Pegoretti A. Fatigue resistance of basalt fibers-reinforced laminates. *J Compos Mater* 2012; 46: 1773–1785.
21. Jacob S, Suma KK, Mendez JM, et al. Reinforcing effect of nanosilica on polypropylene–nylon fibre composite. *Mater Sci Eng B* 2010; 168: 24–249.
22. Isitman NA, Gunduz HO and Kaynak C. Nanoclay synergy in flame retarded/glass fibre reinforced polyamide 6. *Polym Degrad Stabil* 2009; 94: 2241–2250.
23. Vlasveld DPN, Parlevliet PP, Bersee HEN, et al. Fibre–matrix adhesion in glass-fibre reinforced polyamide-6 silicate nanocomposites. *Compos Part A Appl Sci Manuf* 2005; 36: 1–11.
24. Dorigato A, Pegoretti A and Penati A. Linear low-density polyethylene–silica micro- and nanocomposites: Dynamic rheological measurements and modeling. *Exp Polym Lett* 2010; 4: 115–129.
25. Fukushima H. *Graphite nanoreinforcements in polymer nanocomposites*. East Lansing, MI: Michigan State University, 2003.
26. James E. *Polymer data handbook*. New York: Oxford University Press, 1999.
27. Yoo Y, Spencer MW and Paul DR. Morphology and mechanical properties of glass fiber reinforced Nylon 6 nanocomposites. *Polymer* 2011; 52: 180–190.
28. Kelly A and Tyson WR. Tensile properties of fibre-reinforced metals. *J Mech Phys Solids* 1965; 13: 329–350.
29. Vaxman A, Narkis M, Siegmann A, et al. Short-fiber thermoplastics composites: Fiber fracture during melt processing. In: Nicolais L and Borzacchiello A (eds) *Wiley encyclopedia of composites*, 2nd ed. Hoboken, NJ: John Wiley & Sons, 2012.
30. Kwiatkowski D, Nabialek J and Gnatowski A. The examination of the structure of PP composites with the glass fibre. *Arch Mater Sci Eng* 2007; 28: 405–408.
31. Zeng QH, Yu AB and Lu GQ. Multiscale modeling and simulation of polymer nanocomposites. *Prog Polym Sci* 2008; 33: 191–269.
32. Spencer MW, Cui L, Yoo Y, et al. Morphology and properties of nanocomposites based on HDPE/HDPE-g-MA blends. *Polymer* 2010; 51: 1056–1070.
33. Karevan M, Pucha RV, Bhuiyan MA, et al. Effect of interphase modulus and nanofiller agglomeration on the tensile modulus of graphite nanoplatelets and carbon

nanotube reinforced polypropylene nanocomposites. *Carbon Lett* 2011; 11: 325–331.
34. Tsai SW and Pagano NJ. Composite materials workshop. In: Tsai SW, Halftone JC and Pagano NJ (eds) *Progress in Materials Science series*. Stamford, CT: Technomic, 1968, p.233.
35. Christensen RM and Waals FM. Effective stiffness of randomly oriented fibre composites. *J Compos Mater* 1972; 6: 518–535.
36. Medeiros Araujo T and Pegoretti A. Liquid crystalline single-polymer short-fibers composites. *Compos Interf* 2013; 20: 287–298.
37. Hamma A, Kaci M, Mohd Ishak ZA, et al. Starch-grafted-polypropylene/kenaf fibres composites. Part 1: Mechanical performances and viscoelastic behaviour. *Compos Part A Appl Sci Manuf* 2014; 56: 328–335.
38. Banik K, Karger-Kocsis J and Abraham T. Flexural creep of all-polypropylene composites: Model analysis. *Polym Eng Sci* 2008; 48: 941–948.